Journal Name

ARTICLE

Improvement of the electron collection efficiency in porous hematite using a thin iron oxide underlayer: towards efficient all-iron based photoelectrodes†

Received 00th January 20xx,
Accepted 00th January 20xx

DOI: 10.1039/x0xx00000x

www.rsc.org/

Nicola Dalle Carbonare,[a] Stefano Carli,[a] Roberto Argazzi,[b] Michele Orlandi,[c] Nicola Bazzanella,[c] Antonio Miotello,[c] Stefano Caramori,*[a] Carlo A. Bignozzi*[a]

Different approaches have been explored to increase the water oxidation activity of nanostructured hematite (α-Fe_2O_3) photoanodes, including doping with various elements, surface functionalization with both oxygen evolving catalysts (OEC) and functional overlayers and, more recently, the introduction of ultrathin oxide underlayers as tunneling back contacts. Inspired by this latter strategy, it is presented here a photoanode design with a nanometric spin-coated iron oxide underlayer coupled with a mesoporous hematite film deposited by electrophoresis. The electrodes equipped with the thin underlayer exhibit a four-fold improvement in photoactivity over the simple hematite porous film, reaching a stable photocurrent density of ca. 1 mA cm^{-2} at 0.65 V versus the saturated calomel electrode (SCE) at pH 13.3 (NaOH 0.1 M) under air mass (AM) 1.5G illumination. Further improvement to 1.5 mA cm^{-2} is observed after decoration of the hematite surface with a Fe(III)-OEC. These results demonstrate that by combining different iron oxide morphologies it is possible to improve the selectivity of the interfaces towards both electron collection at the back contact and hole transfer to the electrolyte, obtaining an efficient all-iron based photoelectrode entirely realized with simple wet solution scalable procedures.

Introduction

Photoelectrochemical water splitting represents a sustainable way to obtain carbon-free fuel from water using solar light as energetic input, taking advantage of the immense solar power constantly reaching the earth surface in order to generate molecular hydrogen and oxygen.[1,2]

Many metal oxide semiconductors play a central role in the building of photoanodes,[3,4] designated to the photo-oxidation of water, due to the fulfilment of some fundamental requirements: (i) suitable band gap for the absorption in the near UV and visible region of the solar spectrum; (ii) correct position of the Valence Band (VB) edge with respect to O_2/H_2O potential and (iii) stability in water electrolyte solutions at appropriate pH.

In this context, nanostructured hematite (α-Fe_2O_3), due to its band gap of ca. 2.2 eV (corresponding to λ = 560 nm) and a VB edge more positive than the H_2O oxidation potential, has become in the last years one of the most popular semiconductor employed for the fabrication of cheap and earth-abundant photoanodes.[5,6] Despite these essential characteristics, hematite is known to suffer high recombination rates mainly involving trapped charge carriers,[7,8] and very slow hole-transfer kinetics from the bulk oxide to the solution.[9,10] Strategies to overcome these negative features commonly involve n-doping with various elements (e.g. Pt, Sn, Si, Cd)[11-14] designed to increase electron conductivity of the material and functionalization of the electrode surface with oxygen evolving catalysts (OEC) (e.g. IrO_2, Co-Pi, Fe-OEC),[15-17] to improve water oxidation kinetics resulting either in a photoanodic-onset shift to less positive values or in the enhancement of the photocurrent response, or both. Passivation of surface states (that act as recombination centres) using a conformal overlayer such as Al_2O_3[18,19] or In_2O_3[20] is another approach to reduce the overpotential required to trigger photocurrent generation.

More recently, a new strategy to promote photoconversion efficiency of hematite electrodes has been developed, involving thin films of hematite deposited over ultrathin layers of different oxides that, having a conduction band significantly higher than that of hematite, act as tunneling junction. Usually such underlayers are used in combination with very thin hematite films (10-30 nm), that do not guarantee high Light Harvesting Efficiency (LHE), but are desirable due to the reduction of the photogenerated holes path to reach the

[a] Department of Chemical and Pharmaceutical Sciences, University of Ferrara, via Fossato di Mortara 17-27, 44121 Ferrara, Italy. E-mail: cte@unife.it, g4s@unife.it; Fax: +39 0532 240407; Tel: +39 0532 455146.
[b] CNR/ISOF c/o Department of Chemical and Pharmaceutical Sciences, University of Ferrara, via Fossato di Mortara 17-27, 44121 Ferrara, Italy.
[c] Department of Physics, University of Trento, via Sommarive 14, I-38123 Povo, Trento, Italy.

† Electronic Supplementary Information (ESI) available: SEM images, EDS analysis, Micro-Raman spectra, XRD, chronoamperometries, statistics of the *J-V* response, IPCE, photovoltage decays, plot reporting R_3, CPE2 and $\delta J/\delta V$ values, Nyquist and Mott-Schottky plots and PL spectra of different samples. See DOI: 10.1039/x0xx00000x

semiconductor-liquid junction (SCLJ) from the bulk. This allows holes to be transferred to the solution with minimized recombination losses, finding a compromise between deep light penetration depth (α^{-1} = 118 nm at λ = 550 nm)[21] and very short hole diffusion length (2-4 nm).[22] Improvement of the water oxidation activity has been observed adopting different ultrathin oxide underlayers. Steier et al.[23] observed that doping hematite with Si and Nb diffusing from underlayers of SiO_x and Nb_2O_5, improves the photoanodic performance of 10-15 nm ultrasonic spray pyrolysed (USP) hematite films. SiO_x[24] and Ga_2O_3[25] are also responsible for a beneficial increase in hematite crystallinity due to the reduction of the unfavorable mismatch between the FTO and hematite lattices. Similar results have been obtained by Zhang et al.[26] with TiO_2 and by Zandi et al.[27] with Ga_2O_3 and Nb_2O_5 underlayers, who demonstrated how the ~3 times higher crystallinity of 18 nm atomic layer deposited (ALD) hematite film results in stronger light absorption closely related to photocatalytic water oxidation performance. In spite of the still debated exact physical effect of the oxide underlayer, it is reasonable to assume that the electronic effect should also be related to a reduction in electron/hole recombination at the FTO/hematite interface due to the insulating nature of the underlayer. In 2008, Liang et al.[28] have reported a beneficial effect for both the reproducibility and the photocurrent efficiency of 200 nm spray pyrolised and silicon-doped hematite using a 5 nm spray pyrolised SnO_2 underlayer.

Following this latter approach, we have explored the coupling of a non-insulating thin underlayer of spin-coated α-Fe_2O_3 (HTL) with an electrophoretically deposited mesoporous α-Fe_2O_3 film (MPH), realizing distinct layers cooperating to improve the charge separation in photoelectrodes entirely realized with iron based materials. The presence of a ≈30 nm thin underlayer results in a four fold enhancement of the photocurrent generated by the hematite electrode under a positive potential bias, reaching ca. 1 mA cm^{-2} under 0.65 V vs SCE in NaOH 0.1 M (pH 13.3) and further improves to 1.5 mA cm^{-2} after the decoration with an iron(III)-OEC. A combination of DC electrochemical techniques and electrochemical impedance spectroscopy (EIS) analysis was employed to gain a mechanistic understanding of the improved charge separation in the combined HTL-MPH electrodes, showing that the development of a depletion region across the photoactive films, made possible by the HTL, is responsible for the increased electron collection efficiency. Furthermore, at the SCLJ the iron(III) catalyst is able to trap holes in reactive sites exposed to the electrolyte favouring their transfer to the solution. It is thus demonstrated that the cooperation of different layers of the same type of oxide (thin crystalline, porous crystalline and amorphous iron oxide) allows to tune the performance of the electrode, allowing to extract a significant amount of charge (ca. 20 % of Absorbed Photon-to-current Conversion Efficiency, APCE, at 360 nm and 0.6 V vs SCE in NaOH 0.1 M) from a 300 nm thick solution processed mesoporous film with excellent light harvesting capabilities, thus realizing an efficient all-iron based photoelectrode

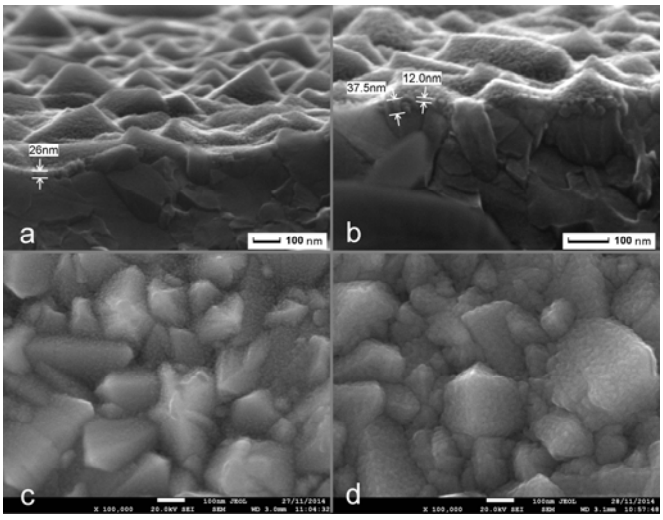

Fig. 1 Cross sectional SEM images of (a, b) HTL-3 sample and top-view SEM images of (c) HTL-1 and (d) HTL-4 samples.

obtained with scalable wet solution procedures and without addition of external dopants.

Results and discussion

The α-Fe_2O_3 thin underlayer (HTL) was prepared with an aqueous $FeCl_3$ precursor modified with a polyethylenglycol (PEG) polymer by spin-coating over FTO glasses followed by annealing at 550°C. Sol-gel based procedures employing spin coating technique have been successfully applied in the years to prepare thick un-doped and doped hematite photoanodes characterized by reasonable photocatalytic performances.[29-31] In our cases we limited the spin coating process to the formation of a thin layer (few nm) which would serve as a host for the subsequent nanoparticles deposition aimed at the formation of a thicker film tasked with the quantitative absorption of suitable energy photons. The number of spin coating runs was repeated from one to four times to yield HTL-1-4 type substrates (Fig. S1, ESI†). SEM cross sectional views of HTL-3 (Fig. 1a-b) shows a quite-uniform conformal coverage of the larger FTO crystallites by nanometric grains of iron oxide of the size of ca. 10-12 nm (Fig. 1b), filling up the gaps between the FTO plates. HTL substrates, although characterized by discernible features due to the aggregation of single substructures of estimated size < 5 nm, retain a quite compact morphology corroborated by a lower roughness factor (15) with respect to the mesoporous α-Fe_2O_3 (MPH) samples (25). The repetition of subsequent spin coating cycles increases the FTO coverage by the α-Fe_2O_3 layer, as can be appreciated from SEM imaging (Fig. 1c-d).

The deposition of the mesoporous α-Fe_2O_3 film (MPH) was carried out according to an electrophoretic procedure,[32] which was selected as a fast, scalable and cost effective method for obtaining porous hematite electrodes, by applying 10 V to either FTO or HTL samples immersed in a colloidal suspension of hydrothermally grown Fe_2O_3 nanoparticles. The subsequent annealing at 550°C yields a crystalline hematite film. XRD carried out on the hematite powder used for the

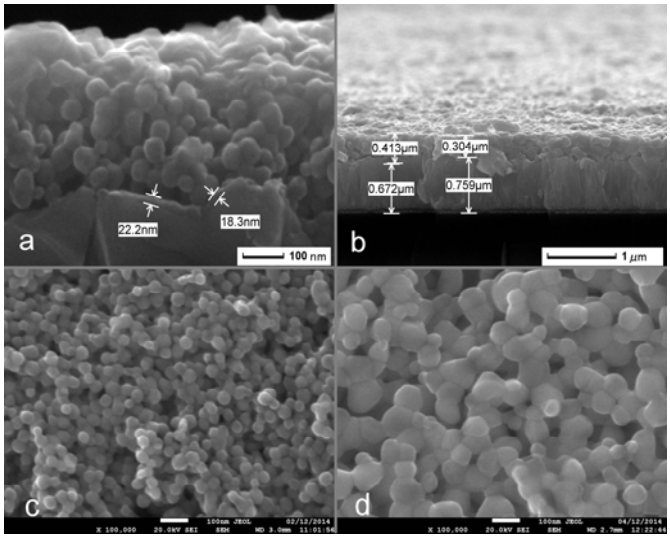

Fig. 2 Cross sectional SEM images of MPH electrophoretically deposited over HTL-3 and annealed at (a) 550°C and (b) 800°C. After activation at 800°C for 20 minutes it is more difficult to distinguish the discontinuity between HTL-3 and MPH layers. Top-view SEM images of MPH deposited over HTL-3 and annealed at (c) 550°C and (d) 800°C.

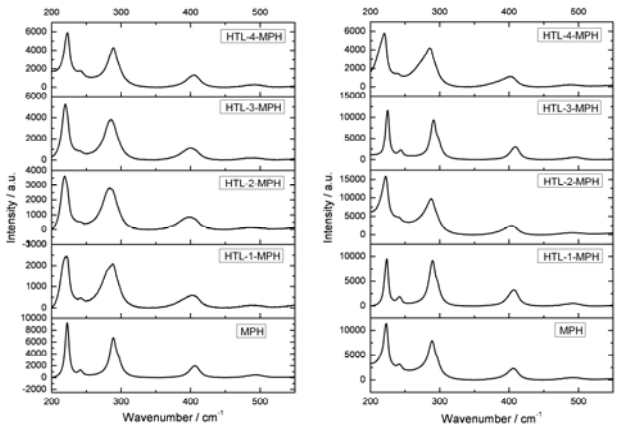

Fig. 3 Micro-Raman spectra of MPH deposited on FTO (MPH) and on HTL-1-4 before (left) and after (right) annealing at 800°C. Besides characteristic hematite modes (229, 295, 414 cm^{-1}), minor peaks are present at: 249, 500, 615, 660 and 1320 (second order) cm^{-1}. For this reason all spectra are reported in the range 200-550 cm^{-1}.

electrophoretic deposition revealed that after the 180 °C growth in autoclave the particles already show a diffraction pattern consistent with the presence of hexagonal hematite (Fig. S2, ESI†). The diffraction peaks however gain intensity after the 550 C° and 800 C° treatments, indicating both an improvement in crystallinity and an increase of the coherent scattering domains. Such features are consistent with the morphological changes observed by SEM imaging on the photoelectrodes.

After MPH deposition, the HTL-3, with an estimated thickness of 32 ± 6 nm (Table S1, ESI†), is still distinctly visible under the mesoporous α-Fe_2O_3 prolate particles (Fig. 2a) forming a film with a thickness varying in the range of 300-400 nm (Fig. 2b). After 800°C activation of the electrodes the morphology of the MPH film changes, showing the growth and increased necking of partially fused spheroidal nanoparticles whose diameter ranges between 60 and 100 nm (Fig. 2c-d and Fig. S3, ESI†). The presence of the underlying HTL does not seem to have large repercussions on the necking of the mesoporous nanoparticles upon 800°C annealing compared to MPH alone directly deposited on FTO (Fig. S4, ESI†). The cross sectional energy dispersive analysis (Fig. S5, ESI†), carried out to monitor possible changes in the elementary composition of the photoactive film, reveal, within the sensitivity of the technique, a similar tin concentration profile in the hematite layer before and after the 800°C activation step, suggesting that the major impact of high temperature activation is related to the improvement of the electrical contacts across the mesoporous film. Estimation of the doping density (vide infra) carried out by Mott-Schottky analysis corroborates this indication showing a relatively low doping level of hematite. The α-Fe_2O_3 crystalline phase of MPH cast over bare FTO or HTL is clearly identified by Micro-Raman analysis showing the characteristic hematite modes at 229, 295, 414 cm^{-1},[33] displaying similar relative ratio regardless of the underlying substrate (Fig. 3). A similar Raman signature is present in the HTL layers (Fig. S6, ESI†), even though for the HTL-1 sample a complete deconvolution of the hematite response from the FTO background is not possible, due to the very low thickness of the hematite film and incomplete coverage of the FTO. Differently from the effect reported with Nb_2O_5 underlayer, resulting in improved crystallinity correlated to enhanced photocatalytic properties of ALD deposited hematite,[27] we did not observe a substantial improvement of the crystallinity of the MPH film in the presence of HTL, based on the comparative width and intensity of the Raman signals (Fig. 3), which instead reveal after 550°C annealing a broader shape of hematite main peaks. The crystallinity of the surface is however recovered and brought at comparable levels after the 800°C treatment. XRD analysis, more sensitive than Raman to the bulk properties of the material, carried out on the MPH and HTL-MPH films (Fig. S7, ESI†), confirmed the similar crystalline nature of the two samples.

The absorption spectra further confirm the hematite nature of the HTL and MPH films, showing the two characteristic bands at 535-540 and 385 nm[34] (Fig. 4a-b). In the case of MPH electrode the absorption saturates at λ < 420 nm, reaching optical densities > 2.5 and allowing a quantitative absorption of photons with λ < 550 nm. The optical absorption depths (α^{-1} in nm) extracted from the absorption spectra using the eqn (1), where *A* is the background subtracted absorbance at 550 nm and *x* is the film thickness (nm), estimated by cross sectional SEM images, yield coherent values of 111 and 117 nm^{-1} for HTL-3 and HTL-3-MPH in good agreement with reported values for hematite.[21]

$$A = \alpha \cdot x \cdot 2.3 \quad (1)$$

The absorption of the HTL, ranging from 0.13 (HTL-1) to 0.4 (HTL-4) increases in an almost linear fashion with the first three spin coating runs (Fig. S8, ESI†), starting to reach a plateau at the fourth spin coating cycle, probably corresponding to a complete coverage of the FTO substrate. The absorbance of the combined HTL-MPH electrode is

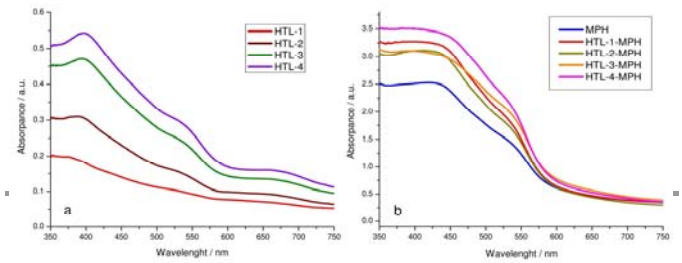

Fig. 4 Absorption spectra of (a) HTL-1-4 spin coated on FTO and (b) MPH deposited on FTO (blue line) and on HTL-1-4 samples.

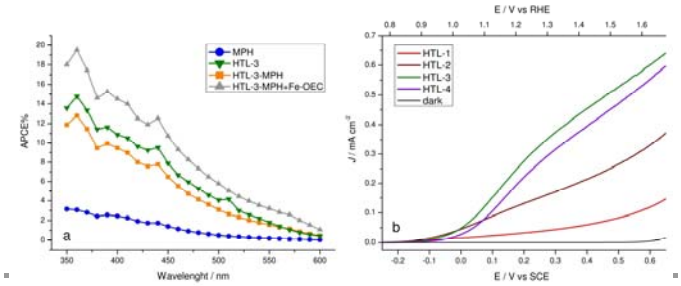

Fig. 6 (a) APCE spectra recorded at 0.6 V vs SCE in NaOH 0.1 M (pH 13.3) of MPH, HTL-3 and HTL-3-MPH with and without Fe-OEC. (b) *J-V* curves under continuous illumination (100 mW cm^{-2}, AM 1.5G) of HTL-1 to -4 samples in NaOH 0.1 M (pH 13.3).

superior to the additive contribution of MPH and HTL, reflecting a more favourable interaction of the hematite nanoparticles with the HTL layer, leading to a denser and closely packed porous film whose thickness is, however, comparable to that of MPH on bare FTO (Fig. S9, ESI†).

The presence of HTL improves the photoanodic activity of the hematite electrodes, with the best performance observed with MPH deposited over HTL-3 sample (Fig. 5a). The photoanodic current at 0.65 V vs SCE reaches 0.95 mA cm^{-2} under 1 sun illumination in 0.1 M NaOH, producing a 4-fold enhancement with respect to MPH deposited directly on FTO, limited to just 0.23 mA cm^{-2} at the same potential. In the presence of the Fe(III)-OEC,[17,35] which does not alter the absorption profile of the electrode, a further enhancement of the photocurrent response is observed, reaching 1.5 mA cm^{-2} at 0.65 V vs SCE (Fig. 5b). There is not, however, a discernible cathodic shift of the photoanodic threshold between the samples, placed in every case around -0.05 V vs SCE. The shuttered *J-V* curves in the presence of the Fe(III) catalyst show rectangular shaped photoanodic transients starting from 0.2 V vs SCE indicating improved rectifying properties of the SCLJ in the presence of both the catalyst and the HTL-3 (Fig. 5b). Compared to the photoanodic plateau value, the relative intensity of the cathodic spikes is reduced in HTL-MPH type electrodes compared to MPH, suggesting, in the former, a lower extent of recombination occurring at the FTO/hematite interface.

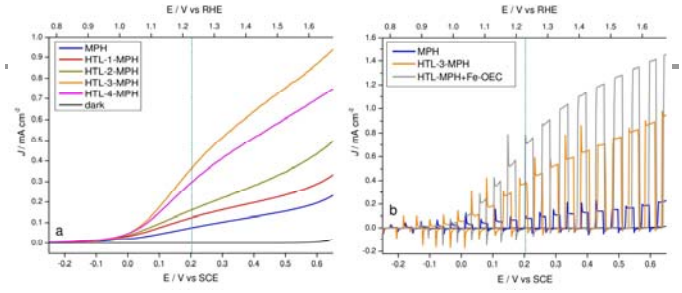

Fig. 5 (a) *J-V* curves under continuous illumination of MPH deposited on FTO (blue line) and over HTL-1-4 samples (colored lines). (b) *J-V* curves under shuttered illumination of MPH deposited on FTO (blue line) and HTL-3-MPH electrode before (orange line) and after (grey line) functionalization with Fe-OEC. Data collected with AM 1.5 G illumination, 100 mW cm^{-2} in NaOH 0.1 M (pH 13.3). The dotted vertical bar in *J-V* plots represents water oxidation potential at working pH value (1.23 V vs RHE).

The appearance of transient features in the -0.2/-0.1 V vs SCE interval is consistent with the photoanodic threshold evaluated under steady state conditions, providing a first approximate estimate of the flat band potential (-0.2 V vs SCE) of these hematite electrodes at pH 13.3. All samples show an excellent stability under prolonged operating conditions (Fig. S10, ESI†), ruling out photocorrosion and degradation of the materials. The procedures used to assemble the single iron oxide structures (HTL, MPH and Fe-OEC) in the final device reveal a very good reproducibility with reference to the *J-V* response (Fig. S11, ESI†), considering that all the preparative steps involve solution based techniques.

The APCE (APCE=IPCE/LHE) spectra recorded at 0.6 V vs SCE confirm the marked superiority of the HTL-3-MPH type electrodes, producing a quadruple internal quantum yield with respect to simple MPH. The presence of the catalyst further increases the quantum yield to ca. 20 % at 360 nm (Fig. 6a). The APCE spectra, being normalized for the LHE, confirm the intrinsic ability of the HTL-3-MPH electrodes to achieve a superior charge separation and collection over the MPH layer. It is interesting to note that the combined HTL-3-MPH electrode produces, at longer wavelengths (> 500 nm), APCEs comparable to that of the much thinner HTL-3 alone, whose nanometric thickness should allow for improved electron collection of charge carriers having short diffusion length.[36] Indeed, the HTL-3 is able to produce respectable performances, despite of the modest LHE, generating limiting photocurrents of the order of 0.65 mA cm^{-2} at 0.65 V vs SCE by converting mostly high energy photons having short penetration depths (Fig. 6b). HTL performance varies in the order HTL-1 < HTL-2 < HTL-3 > HTL-4.

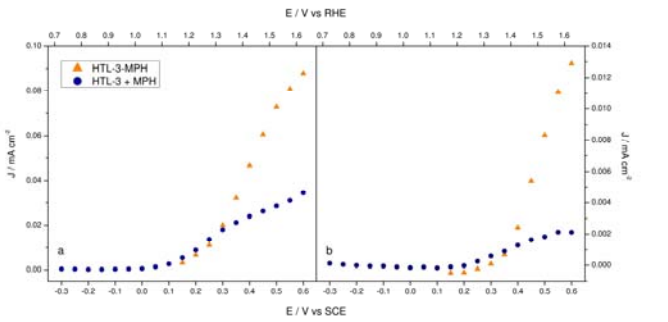

Fig. 7 *J-V* curve of HTL-3-MPH (orange triangles) and sum of the separate response of MPH and HTL-3 (navy circles) recorded with a (a) 550 and (b) 600 nm monochromatic light in NaOH (0.1 M, pH 13.3).

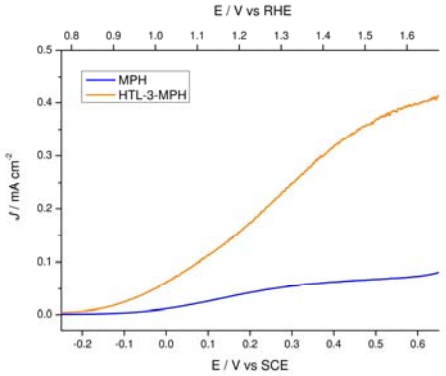

Fig. 8 *J-V* curves recorded under electrolyte side illumination (100 mW cm^{-2}, AM 1.5 G) of MPH (blue) and HTL-3-MPH (orange) in NaOH (0.1 M, pH 13.3)

Thus in our conditions HTL-3 represents the best compromise between FTO coverage, thickness compatible with the short hole diffusion length and light harvesting properties.

The addition of the catalyst directly onto the HTL-3 sample improves only slightly the photoactivity, with an overall current limited to ca. ½ of that obtained with the combined electrode, HTL-3-MPH, due to a an insufficient harvesting of long wavelength photons (Fig. S12, ESI†).

Although in the combined electrode the HTL layer can directly contribute to the performance of HTL-MPH, by harvesting and converting a fraction of high energy photons, its conversion efficiency, once covered by MPH, is essentially not known. In general, with respect to an equivalent bare HTL film presenting its whole surface exposed to the electrolyte, it can be expected a lower direct photon to electron conversion of HTL in the HTL-MPH assembly where the coverage by MPH limits the amount of HTL surface in contact with the electrolyte. The monochromatic *J-V* characteristics recorded both at 550 and at 600 nm (Fig. 7a-b), where the absorption of the HTL layer is negligible against photons having a penetration depth > 110 nm, reveal a distinct advantage of the combined HTL-3-MPH substrate generating from ca. x 2 to × 5 increase in photocurrent with respect to the sum of the separate contributions of HTL-3 and MPH. This is confirmed by IPCE spectra (Fig. S13, ESI†), showing a larger response of the combined layer to photons having λ > 500 nm. Thus, a substantially higher fraction of charge carriers, generated within the MPH layer, is able to reach the electron collector in the presence of HTL, indicating that the performance of the combined photoelectrode is not simply the superposition of the performances of the two distinct layers but also results from more subtle effects in charge separation mechanism.

J-V curves recorded under electrolyte-side illumination (AM 1.5 G)(Fig. 8), where most of the charge carriers are generated within the strongly absorbing MPH layer, corroborate the results of the monochromatic measurements with penetrating photons, showing superior charge collection in the HTL-3-MPH electrode, capable to generate photocurrents increased by a × 5 factor with respect to the simpler MPH substrate.

J^2-*V* plots, recorded under different monochromatic illumination wavelengths (350, 360, 550 and 600 nm) (Fig. 9a-d) show a distinct linear dependence for HTL-3 and HTL-3-MPH substrates whereas for MPH on FTO the behaviour shows a more sigmoidal feature (Fig. 9a-b). Linear J^2-*V* plots, according to an approximation of the Gärtner model,[37] valid when the diffusion length of holes (L) is small compared to the depletion length (W), as in the case of hematite,[22] is indicative of a mechanism of charge separation occurring within the space charge layer of the Schottky junction (eqn (2)).[38]

$$J^2 = \Phi_0^2 \alpha^2 \frac{2 \; e \; \varepsilon \; \varepsilon_0}{N}(V - V_{fb}) \qquad (2)$$

This is quite reasonable for a thin layer of relatively compact oxide (HTL), which could be entirely depleted, but it is not necessarily obvious for the porous layer, which indeed, in the case of the MPH substrate alone, does not show a convincing dependence within the framework of the Gärtner approximation.

Photovoltage transients measured in the presence of a reversible redox couple $[Fe(CN)_6]^{4-}/[(Fe(CN)_6]^{3-}$ in which a defined formal potential is varied between 270 and 150 mV (vs SCE), by changing the Fe(III)/(II) ratio (Fig. S14, ESI†), show that both the HTL-3 and HTL-3-MPH are capable of delivering a similar photovoltage (55-60 mV) which decreases 10 mV by reducing the formal potential of the redox couple from 270 to 210 mV, a behaviour expected in the case of formation of a built in potential due to voltage drop within the semiconductor. By contrast, the photovoltage generated by the MPH layer alone is essentially independent of the formal potential of the redox couple, reaching values of 4-6 mV, suggesting Fermi level pinning on surface states rather than potential drop within the space charge. Clearly these data have to be considered with caution since the Fe(II)/Fe(III) couple participates to recombination and hole scavenging events on the semiconductor surface and can alter, through kinetic processes, the final photovoltage value attained by the junction.

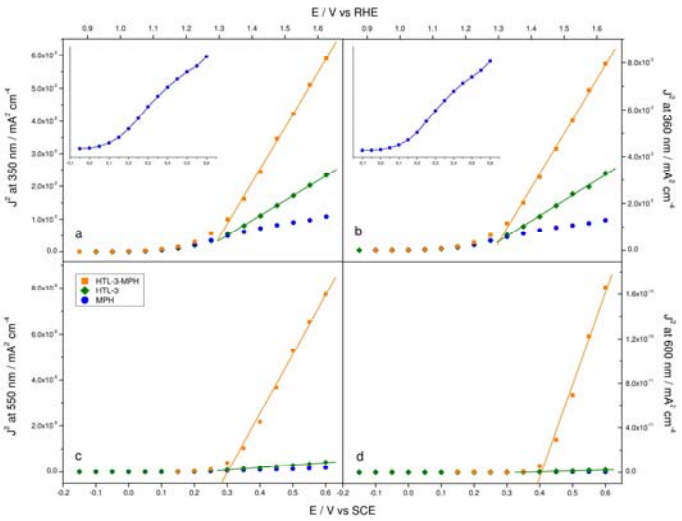

Fig. 9 J^2-*V* plot recorded with a monochromatic light at (a) 350 nm, (b) 360, (c) 550 and (d) 600 nm for MPH (blue circles), HTL-3 (green diamonds) and HTL-3-MPH (orange squares) samples in NaOH (0.1 M, pH 13.3). Insets in graphs (a) and (b) reported a magnification of MPH plot, showing its sigmoidal behaviour.

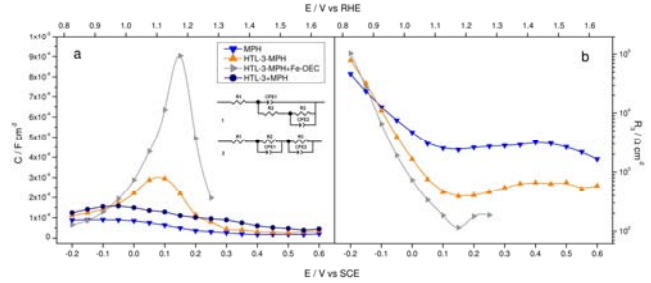

Fig. 10 (a) CPE2 and (b) R_3 plot of MPH and HTL-3-MPH with and without Fe-OEC recorded under AM 1.5G illumination (100 mW cm^{-2}) in NaOH (0.1 M, pH 13.3). In (a) is also reported the sum of the separate chemical capacitance of MPH and HTL-3 as navy circles. Inset in (a): equivalent circuits used for fitting EIS data of (1)HTL-3-MPH and HTL-3-MPH+Fe-OEC and (2) MPH and HTL-3 electrodes. CPE2 represents the non ideal capacitance associated to the semiconductor/electrolyte interface.

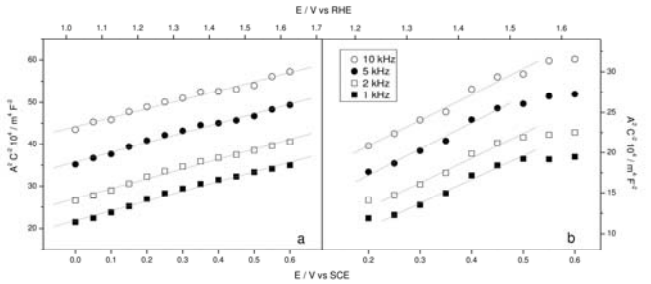

Figure 11. Mott-Schottky plot of (a) HTL-3 and (b) HTL-3-MPH recorded under AM 1.5G illumination in NaOH (0.1 M, pH 13.3) at different frequency (1, 2, 5 and 10 kHz).

Indeed, a further reduction of the formal potential to 150 mV, by introducing a 10 fold excess of Fe(II) with respect to Fe(III), leads to an increase in photovoltage for all substrates under investigation (80 and 100 mV for HTL-3 and HTL-3-MPHand 14 mV for MPH) probably due to improved hole scavenging by the Fe(II). In any case, photopotential measurements are consistent with improved charge separation in HTL-3 and in HTL-MPH type electrodes in the presence of a kinetically facile redox couple, evidencing superior SLCJ rectification properties. This is compatible with the presence of a substantial depletion layer within both the thin film alone (HTL-3) and the combined substrates (HTL-3-MPH).

The charge transfer dynamics of the modified hematite substrates were investigated primarily by scanning reverse potentials along the *J-V* curves under AM 1.5G illumination in the 10 mHz-100 kHz frequency interval, in order to individuate and characterize the active mechanisms responsible for the photocurrent generation. Well-established models for the interpretation of impedance measurements of illuminated and dark α-Fe_2O_3 photoanodes are available in the literature both from works by Peter[39,40] and Bisquert and Hamann.[41]

Typical Nyquist plots of hematite under illumination present two flattened semicircles in the complex plane, having respectively maxima at low (0.1-1 Hz) and high frequency (100-1000 Hz) (Fig. S15, ESI†). Circuital models selected for the EIS data fitting reproduced accurately in all cases (HTL-3, MPH, HTL-3-MPH with and without Fe-OEC) the *J-V* response, as can be appreciated from the excellent correlation between the inverse of the total resistance ($R_{tot} = \sum_{i=1}^{3} R_i$) obtained from EIS data and the derivative of the respective *J-V* curves (Fig. S16, ESI†). In the case of samples where the iron oxide underlayer is present (HTL-3 and HTL-3-MPH with and without Fe-OEC) the circuital model comprises a nested mesh describing both the charge transfer across the depletion layer (R2-CPE1) and the Helmholtz layer (R3-CPE2) (inset 1 in Fig. 10a). In the HTL-3-MPH electrode the major contribution to the total resistance is determined by the interfacial charge transfer resistance at the solid/electrolyte interface (R3), reaching a minimum in correspondence with the inflection point of the *J-V* curves (maximum slope, Fig. S17, ESI†). The capacitance associated with the interfacial charge transfer process (modelled by Constant Phase Element, CPE2) follows a bell shaped distribution, peaking at 0.1 V vs SCE and exhibiting a chemical capacitance behaviour consistent with hole trapping in surface states exposed to the electrolyte, that probably leads to the formation of highly valent iron species responsible for the water oxidation process.[8,41] Indeed, the chemical capacitance of the combined HTL-3-MPH electrode (0.3 mF cm^{-2}) is superior to the simple sum of the individual contributions of HTL-3 and MPH (0.15 mF cm^{-2}) (Fig. 10a), consistent with a superior charge separation and hole trapping capability, corroborating the indications from the monochromatic analysis of *J-V* characteristics. It can be further observed an additional substantial increase in chemical capacitance magnitude, from ca. 0.3 mF cm^{-2} to 1 mF cm^{-2} (Fig. 10a), in the presence of discontinuous islands of amorphous Fe(III) catalyst (HTL-3-MPH sample with Fe-OEC). This effect is also associated to a sharpening of the distribution and to a ca. 100 mV peak shift to more anodic potential, in agreement with the presence of surface species capable to capture and store photogenerated holes (Fig. S17, ESI†).[17] Similar enhancements in the chemical capacitance due to hole trapping have been observed in hematite substrates modified both with Co-Pi[42] and IrO_2.[43] The MPH electrode alone, without the iron oxide thin underlayer, roughly parallels the behaviour already described for the HTL-3-MPH, although its interfacial capacitance values (max. 0.09 mF cm^{-2}) are much lower compared with the HTL-3 MPH and are associated to a considerably higher charge transfer resistance (2400 Ω cm^{-2} for MPH and 380 Ω cm^{-2} for HTL-3-MPH, Fig. 10b). These figures are in agreement with the lower photoelectrochemical performance of MPH, indicating that, in this latter case, the carriers are less capable to escape recombination and be directed to their respective interfaces where they are either collected or injected into the electrolyte.

The comparative analysis of the capacitance in the high frequency region (1 kHz) of HTL-3 and the HTL-3-MPH electrodes show a convincing Mott-Schottky (MS) behaviour with a linear portion providing a doping density of the order of $1.6 \pm 0.3 \cdot 10^{+17}$ cm^{-3} (eqn (3)), consistent with donor densities of un-doped hematite (Fig. 11a-b).[28]

$$N_D = \frac{2}{q \cdot \varepsilon_0 \cdot \varepsilon_{\alpha - Fe_2O_3} \cdot b} \qquad (3)$$

With $\varepsilon_0 = 8.854 \cdot 10^{-12}$ F m^{-1}, $\varepsilon_{\alpha\text{-}Fe2O3} = 32$,[44] $q = 1.610 \cdot 10^{-19}$ C and b= slope of the linear section of Mott-Schottky plots (A^2 C^{-2} vs V). Despite of some high frequency dispersion of the capacitive response of the junction, probably due to microroughness of the FTO/semiconductor/electrolyte

Table 1. Values of flat band potential (V_{fb}) and charge carrier concentration (N_D) of HTL-3 and HTL-3-MPH

	HTL-3		HTL-3-MPH			
	dark		dark		AM 1.5G[a]	
Frequency/ kHz	V_{fb}/ V vs SCE	N_D/ 10^{+17} cm^3	V_{fb}/ V vs SCE	N_D/ 10^{+17} cm^3	V_{fb}/ V vs SCE	N_D/ 10^{+17} cm^3
1	-0.73	1.66	-0.30	1.03	-0.11	1.48
2	-0.93	1.68	-0.36	1.04	-0.17	1.43
5	-1.25	1.65	-0.51	1.06	-0.27	1.34
10	-1.14	2.43	-0.68	1.03	-0.34	1.27

[a] 100 mW cm^{-2} illumination power.

interfaces,[28,45] reasonable values of flat band potentials, in agreement with those estimated by the photocurrent transients, were found with values ranging from -0.11 to -0.34 V vs SCE (Table 1). The observation of a systematic positive shift of the flat band potential of the HTL-3-MPH electrode upon illumination, explainable by a potential drop within the Helmholtz layer caused by surface hole trapping, agrees with previous literature reports.[8] By contrast the MPH layer does not show any MS dependence associated with the high frequency arc, showing essentially a random distribution of the high frequency capacitance with the applied voltage under illumination, indicating that, in this case, the high frequency capacitive response is essentially decoupled from the dynamic processes responsible for photocurrent generation. Likely, the high frequency capacitance could be due to geometric factors (i.e. electrode porosity) or to a passive interface which does not play an active role in photocurrent generation, as confirmed by the associate resistance which is nearly potential independent. For this reason the equivalent circuit used for describing its impedance response is comprised of two separated RC meshes (inset 2 in Fig. 10a). The MS analysis carried out in the dark for the HTL-3 and HTL-3-MPH samples are still consistent with the formation of a depletion layer extending into the hematite material, providing a donor density similar to that obtained under illumination (ca. 10^{+17} cm^{-3}), whereas the MPH electrode was characterized by a linear MS behaviour with substantially different doping density, of the order of 10^{+21} cm^{-3} (Fig. S18, ESI†), attributed to a narrow depletion layer developing into conductive FTO[14] which, under illumination, does not have active participation in the charge separation dynamics within porous hematite. The depletion length calculated with the hematite donor densities extracted from the MS plots yields values of the order of 130 nm at 0.2 V vs SCE (1.23 V vs RHE), indicating that even photons having a deep penetration in the porous layer have considerable chance to generate charge carriers experiencing an electric field which assists charge separation, directing electrons to the back contact and holes to the surface where trapping occurs. This allows to well explain both the enhanced photoanodic response of the hematite electrodes modified with the thin underlayer (HTL-3-MPH) to excitation wavelengths > 500 nm and the increased interfacial hole trapping capacitance. Clearly, the performance of the compact HTL-3 alone is also satisfactory, in relation to its poor light absorption capabilities, due to the fact that this film is most probably entirely depleted and charge carriers are generated within a distance from the collector which is compatible with their short diffusion lengths.

Thus the EIS analysis corroborates the indications obtained from DC photoelectrochemical experiments: in the MPH sample alone, the Fermi level is probably pinned on surface states which could be created during deposition and annealing of Fe_2O_3 nanoparticles on FTO, due to lattice mismatching between these two materials, preventing the possibility of controlling the formation of a depletion layer which would assist charge separation. This effect is largely reduced by the use of the HTL, which, acting as a buffer layer between the porous photoactive layer and FTO, reduces the possibility of trap states formation, consequently avoiding, at least to a sufficient extent, pinning of the Fermi level on defects. The elimination of defects and grain boundaries at the hematite-FTO interface was invoked by Isatomi et al. as the main role played by ultrathin (0-6 nm) ALD deposited Ga_2O_3 underlayers in improving the photoanodic response of modified hematite electrodes.[25]

To further support the role of the HTL layer in the prevention of trap state formation, photoluminescence spectra (PL) have been recorded (Fig. S19, ESI†). It has been shown that the reduction of the amount of surface trap states in hematite photoanodes after overlayer deposition or solution passivation results in an enhancement of photoluminescence,[18,46] since these states behave as nonradiative recombination centres of excitons.[47] The difference emission spectra of HTL-3-MPH and MPH (520 nm excitation light) shows a relatively broad emission peaking at 615-620 nm, consistent with earlier reports of luminescence arising from passivated hematite electrodes,[18] corroborating a decreased defect density induced by HTL acting as buffer later between MPH and FTO.

Conclusions

The photoelectrochemical effect of a thin layer of spin coated crystalline hematite acting as a host surface for the electrophoretic deposition of mesoporous Fe_2O_3 nanoparticles was explored. The new combined hematite photoanode, entirely obtained with wet solution methods and without introduction of external dopants, exhibits a four-fold improvement in photoactivity over the simple hematite mesoporous film, reaching a stable limiting photocurrent density of ca. 1 mA cm^{-2} at 0.65 V vs SCE under AM 1.5G illumination. The improved performance results in part from the individual properties of the two layers, in which the thin underlayer, efficient in charge collection, captures mostly high energy photons while the thicker mesoporous layer harvests longer wavelength visible radiation.

However, the photoelectrochemical response of the combined HTL-MPH electrode is not the simple superposition of the properties of the two materials, as can be revealed by the improved charge separation and collection observed upon

excitation with deeply penetrating photons, (α^{-1} (λ) > 100 nm) generating carriers mostly in the thick porous film. The combination of DC and EIS indicates that the electric field within a depletion layer, extending for a substantial fraction of the whole HTL-MPH electrode, has a role in driving the charge carriers towards the two different interfaces, where they are collected (electrons at FTO) or trapped in reactive states and transferred to the electrolyte (holes). This observation is consistent with the presence of the HTL that, acting as a buffer layer between the porous photoactive hematite film and FTO, can reduce the possibility of trap states and grain boundaries formation avoiding pinning of the Fermi level on defects.

This mechanism of action of the thin host underlayer, which contrary to other literature approaches, is transparent to conduction band electrons, is different from those reported for other semiconductor oxides acting as insulating/tunneling junctions, and may represent a convenient scalable method to improve the selectivity of the interfaces to the respective charge carriers in sol-gel hematite photoelectrodes. A further improvement to a photoanodic limiting value of 1.5 mA cm^{-2} at 0.65 V vs SCE is observed after decoration of the hematite surface with an Fe(III)-OEC, representing one of the highest photocurrent values for un-doped all-iron based photoelectrodes entirely realized with simple wet solution procedures. Further improvement of the catalyst coating, by achieving a more homogeneous and conformal surface coverage may further improve the photoelectrochemical response of these substrates.

Experimental

Materials

$FeCl_3 \cdot 6H_2O$ (≥99%) and NaOH (98%) were purchased from Alfa Aesar. Polyethyleneglycol Bisphenol A Epichlorohydrin Copolymer (mol wt 15000-20000 Da), anhydrous sodium acetate (≥98%), iodine (≥99.8%) and Orange II sodium salt (4-(2-Hydroxy-1-naphthylazo)benzenesulfonic acid sodium salt, dye content ≥85%) were purchased from Sigma Aldrich.

FTO glass slides (Fluorine-doped Tin Oxide, TEC 8 Ω/cm^2, Hartford Glass, 2.5 x 3 cm) were cleaned by successive 30 minutes ultrasonic treatments in acetone, ethanol, aqueous Alconox® (Sigma Aldrich) solution and distilled water and then blown dry with a warm air stream. A portion of the slides was then masked with KAPTON tape (Tesa) to preserve an uncovered zone for the electric contact.

α-Fe_2O_3 thin underlayer (HTL) deposition

$FeCl_3 \cdot 6H_2O$ (0.54 g) was dissolved in DI water (20 mL) and then Polyethyleneglycol Bisphenol A Epichlorohydrin Copolymer (0.54 g) was added under gentle stirring to avoid the formation of bubbles. The solution was spin coated onto FTO glass (1000 rpm for 9 seconds and 2000 rpm for 30 seconds) with a KV-4A Spin Coater (Chemat Technology). After every spin coating cycle the glass slide was annealed at 550 °C for 15 minutes in air. Spin coating cycles were repeated for 1, 2, 3 and 4 times leading to the HTL-1-4 type electrodes.

Mesoporous α-Fe_2O_3 film (MPH) deposition

Mesoporous α-Fe_2O_3 was electrophoretically deposited on either FTO glass or on HTL samples following a literature procedure.[32] Briefly, in a Teflon beaker $FeCl_3 \cdot 6H_2O$ (0.55 g) was dissolved in a mixed solution of ethanol (20 mL) and water (5 mL) and then sodium acetate (0.8 g) was added. The beaker containing the dark brown solution was capped with Teflon tape and put in a steel autoclave at 180 °C for 12 hours. The autoclave was cooled down at room temperature and the resulting red powder was first washed several times with water and acetone and then suspended in acetone (50 mL). To a sample of this colloidal solution (5 mL), iodine (20 mg) and acetone (45 mL) were added, mixed in an ultrasonic bath for ten minutes and used for the electrophoretic deposition of iron oxide nanoparticles. FTO slides and HTL samples were immersed (2 x 3 cm) in the colloidal solution and polarized at 10 V in two electrode configuration (a bare FTO glass was used as counter electrode at a distance of 0.8 cm) for 35 seconds with an Eco Chemie Autolab PGSTAT 302/N electrochemical work-station. The nanoparticles deposited at the negative electrode resulting in a homogeneous red coating. The electrodes were washed with acetone and then annealed first at 550 °C for 1 hours and then at 800 °C for 20 minutes in air. Each slide was cut to 1 x 1 cm active surface electrodes used for characterization.

Fe(III) Oxygen Evolving Catalyst (OEC) deposition

HTL-3-MPH electrodes were functionalized with iron(III) hydrous oxide (Fe-OEC) by using a ten cycle SILAR (Successive Ionic Layer Adsorption and Reaction) procedure. Each cycle consisted in the dipping of the electrode (1 cm^2 active surface) in a $FeCl_3 \cdot 6H_2O$ aqueous solution (50 mM) and then in NaOH (0.1 M). After each cycle the electrode was rinsed with abundant distilled water and, upon completion of the 10 cycles, annealed at 200 °C for 20 minutes in air.

MicroRaman spectroscopy

All measurement were performed on a Horiba LabAramis setup equipped with a HeNe 633 nm laser as source and a confocal microscope coupled to a 460 mm-focal length CCD-based spectrograph equipped with a PC-controlled four interchangeable gratings-turret. In the range between 450 nm and 850 nm, the wavenumber accuracy is 1 cm^{-1} with the 1800 l/mm grating. The laser power is 15 mW and the maximum spot size is 5 μm. An accumulation number of 10 and an exposure time of 7 s were employed for all measurements except for HTL-1 and its FTO reference, where the exposure time was 10 s and the accumulation number 30.

SEM analysis

Scanning electron microscopy (SEM) was used to analyze the morphology and thickness of films. The surface of the films was analyzed by a JEOL JSM-7001F field effect gun (FEG-SEM) apparatus at 20 keV beam energy. SEM apparatus is equipped with an Energy Dispersive X-ray Spectroscopy detector (EDXS,

Oxford INCA PentaFETx3). Working Distance (WD) was maintained between 3 to 8 mm. Surface morphology images were acquired in top-down and tilted mode whereas cross section analysis were performed putting the films on a 90° stub. Energy dispersive x-ray analysis (EDS) was performed in line-scan mode on two different sections of MPH sample before and after 800°C annealing. The beam energy was 15 KeV and the working distance 10 mm.

UV-Visible spectra

UV-Visible spectra were recorder with a Cary 300 UV-Visible spectrophotometer (Agilent Technologies) in the 750-350 nm region with a home-made glass support for the electrodes.

Roughness Factor

Roughness factor (RF) of HTL-3, MPH and HTL-3-MPH samples was calculated as the ratio between the real surface area and the geometric area of the electrode (1 cm^2). The real surface area has been determined by the absorption of the azo-dye Orange II.[48,49] The electrodes (with the bare FTO portion cover with Kapton tape) were immersed for 15 minutes in a Orange II water solution (1.5 mM, pH 3.5) and then washed with NaOH (1.5 mL, 1 M). The concentration of the dye absorbed to the film was obtained by measuring the optical density at 454 nm. Considering that at the operating conditions the Orange II dye is expected to form a monolayer on the iron oxide surface occupying an area of 40 nm^2 per dye molecule, the RF factor calculated is 15 for HTL-3, 25 for HTL-3-MPH and 25 for MPH on FTO.

DC Photoelectrochemical measurements

J-V curves, chronoamperometry and chronopotentiometry measurements were carried out in a three electrode configuration cell using a platinum and a saturated calomel electrode (SCE) as counter and reference electrode, respectively, connected to an Eco Chemie Autolab PGSTAT 302/N electrochemical work-station. The working electrode was irradiated using an ABET solar simulator (AM 1.5G, 100 mW cm^{-2}) from the FTO side and the illuminated area was 1 cm^2.

J-V curves were recorded at a scan speed of 20 mV s^{-1} by scanning the bias region between the open circuit voltage (under illumination) and 0.65 V vs in NaOH (0.1 M, pH 13.3). Shuttered *J-V* curves were obtained using an Oriel manual shutter.

Monochromatic *J-V* curves were recorded using a monochromatic illuminated light source generated by an applied photophysics monochromator (bandwidth 10 nm) coupled to a 175 W Xe lamp (Luxtel) with a spot illuminated area on the electrodes of 0.2 cm^2.

Chronoamperometry was recorded in NaOH 0.1 M (pH 13.3) at 0.6 V vs SCE under 4 hours of continuous illumination.

Chronopotentiometry were carried out in a KOH solution (0.1 M) of $K_4[Fe(CN)_6]$ and $K_3[Fe(CN)_6]$ at different concentration (see Fig. S14, ESI†) using a Oriel manual shutter.

Photoaction Spectra

IPCE spectra were recorded in NaOH (0.1 M, pH 13.3) under a potential bias of 0.6 V vs SCE with the same setup described above for monochromatic *J-V* measurements. The photoanodic current was recorded every 10 nm from 350 and 600 nm on a PGSTAT 30 electrochemical workstation. The incident monochromatic irradiance was measured with a calibrated silicon photodiode (Centronic ASD100-7Q). IPCE was calculated according to eqn (4):

$$IPCE = 1.24\times 10^{-3}(Vm)\frac{J_\lambda(\mu Acm^{-2})}{\lambda(nm)P_\lambda(Wm^{-2})} \quad (4)$$

where J_λ is the photocurrent density at the wavelength λ and P_λ is the incident radiant power.

IPCE data were converted in APCE according to eqn (5):

$$APCE = \frac{IPCE}{1-10^{-A(\lambda)}} \quad (5)$$

Where IPCE(λ) is the incident photon-to-current efficiency at a given wavelength and $A(\lambda)$ is the background subtracted absorbance.

Electrochemical Impedance Spectroscopy(EIS).

Potentiostatic impedance data of photoanodes in the dark and under illumination condition were recorded in the three electrode configuration cell described above in NaOH (0.1 M, pH 13.3). Sample data were obtained from -0.2 to 0.6 V vs SCE at 50 mV intervals employing a FRA2.v10 frequency response analyzer controlled by Nova 1.10. A 10 mV amplitude sinusoidal perturbation (single sine), whose frequency ranged between 100 000 and 0.01 Hz was adopted. The impedance response was fitted using ZView software with the electric equivalents reported in Fig. 10a and Fig. S15 (ESI†) for MPH, HTL-3 and HTL-3-MPH with and without Fe-OEC electrodes. Electrochemical data have also been referred to the reversible hydrogen electrode (RHE) by eqn (6):

$$E_{RHE} = E_{SCE} + 0.059(V)\times pH + 0.241(V) \quad (6)$$

Photoluminescence spectroscopy (PL).

Photoluminescence spectra were recorded with a Edinburgh Instrument equipped with a 900 W Xe arc lamp as excitation source with a 10 nm bandwidth. Solid thin films, placed on dedicated film holders were excited at 520 nm. The emission intensity was optimized by adjusting the angles between the sample, the excitation and the analysis beams by acting on a micromechanical stage. Emission spectra were averaged over 10 scans and subtracted in order to eliminate spurious contributions arising from Raman scattering.

Acknowledgements

Funding from FIRB project N. RBAP11C58Y and PAT (Provincia Autonoma di Trento) project ENAM in cooperation with Istituto MCB of CNR (Italy) is gratefully acknowledged. We are grateful to Mr. Gabriele Bertocchi for XRD measurements.

Notes and references

1 M. X. Tan, P. M. Laibnis, S. T. Nguyen, J. M. Kesselman, C. E. Stanton and N. S. Lewis, *Progress in Inorganic Chemistry*, John Wiley & Sons, New York, 1994.
2 N. S. Lewis and D. G. Nocera, *Procl. Natl. Acad. Sci. U. S. A.*, 2006, **103**, 15729.
3 F. E. Osterloh, *Chem. Soc. Rev.*, 2013, **42**, 2294.
4 R. L. Doyle, I. J. Godwin, M. P. Brandon and M. E. G. Lyons, *Phys. Chem. Chem. Phys.*, 2013, **15**, 13737.
5 K. Sivula, F. Le Formal and M. Grätzel, *ChemSusChem*, 2011, **4**, 432.
6 D. K. Bora, A. Braun and E. C. Constable, *Energy Environ. Sci.*, 2013, **6**, 407.
7 N. J. Cherepy, D. B. Liston, J. A. Lovejoy, H. Deng and J. Z. Zhang, *J. Phys. Chem. B*, 1998, **102**, 770.
8 B. M. Klahr, S. Gimenez, F. Fabregat-Santiago, T. Hamann and J. Bisquert, *J. Am. Chem. Soc.*, 2012, **134**, 4294.
9 B. M. Klahr and T. Hamann, *J. Phys. Chem. C*, 2011, **115**, 8393.
10 S. Pendlebury, M. Barroso, A. J. Cowan, K. Sivula, J. Tang, M. Grätzel, D. Klug and J. Durrant, *Chem. Comm.*, 2011, **47**, 716.
11 Y. S. Hu, A. Kleiman-Shwarsctein, A: J. Forman, D. Hazen, J: N. Park and E. W. Mcfarland, *Chem. Mater.*, 2008, **20**, 3803.
12 Y. Ling, G. Wang, D. A. Wheeler, J. Z. Zhang and Y. Li, *Nano Lett.*, 2011, **11**, 2119.
13 I. Cesar, K. Sivula, A. Kay, L. Zboril and M. Grätzel, *J. Phys. Chem. C*, 2009, **113**, 772.
14 A. Bak, W. Choi and H. Park, *Appl. Catal., B*, 2011, **110**, 207.
15 S: D. Tilley, M. Cornuz, K. Sivula and M. Grätzel, *Angew. Chem. Int. Ed.*, 2010, **49**, 6405.
16 D. K. Zhong and D. R. Gamelin, *J. Am. Chem. Soc.* 2010, **132**, 4202.
17 N. Dalle Carbonare, V. Cristino, S. Berardi, S. Carli, R. Argazzi, S. Caramori, L. Meda, A. Tacca and C. A. Bignozzi, *ChemPhysChem*, 2014, **15**, 1164.
18 F. Le Formal, N. Tétreault, M. Cornuz, T. Moehl, M. Grätzel and K. Sivula, *Chem. Sci.*, 2011, **2**, 737.
19 S: Kment, Z. Hubicka, J. Krysa, D. Sekora, M. Zlamal, J. Olejnicek, M. Cada, P. Ksirova, Z. Remes, P. Schmuki, E. Schubert and R. Zboril, *Appl. Catal., B*, 2015, **165**, 344.
20 T. Hisatomi, F. Le Formal, M. Cornuz, J. Brillet, N. Tétreault, K. Sivula and M. Grätzel, *Energy Environ. Sci.*, 2011, **4**, 2512.
21 K. Itoh and J. O. Bockris, *J. Electrochem. Soc.*, 1984, **131**, 1266.
22 J. H. Kennedy and K. W. Frese, *J. Electrochem. Soc.*, 1978, **125**, 709.
23 L. Steier, I. Herraiz-Cardona, S. Gimenex, F. Fabregat-Santiago, J. Bisquert, S. D. Tilley and M. Grätzel, *Adv. Funct. Mater.*, 2014, **24**, 7681.
24 F. Le Formal, M. Grätzel and K. Sivula, *Adv. Funct. Mater.*, 2010, **20**, 1099.
25 T. Hisatomi, J. Brillet, M. Cornuz, F. Le Formal, N. Tétreault, K. Sivula and M. Grätzel, *Faraday Discuss.*, 2012, **155**, 223.
26 C. Zhang, Q. Wu, X. Ke, J. Wang, X. Jin and S. Xue, *Int. J. Hydrogen Energ.*, 2014, **39**, 14604.
27 O. Zandi, J. A. Beardslee and T. Hamann, *J. Phys. Chem. C*, 2014, **118**, 16494.
28 Y. Liang, C. S. Enache and R. van de Krol, *Int. J. Photoenergy*, 2008, **2008**, 1.
29 F. L. Souza, K. P. Lopes, P. A. P. Nascente and E. R. Leite, *Sol. Energy Mater. Sol. Cells*, 2009, **93**, 362.
30 J. Frydrych, L. Machala, J. Tucek, K. Siskova, J. Filip, J. Pechousek, K. Safarova, M. Vondracek, J. H. Seo, O. Schneeweiss, M. Grätzel, K. Sivula and R. Zboril, *J. Mater. Chem.*, 2012, **22**, 23232.
31 C. Aydın, S. A. Mansour, Z. A. Alahmed and F. Yakuphanoglu, *J. Sol-Gel Sci. Technol.*, 2012, **62**, 397.
32 X. Zong, S. Thaweesak, H. Xu, Z. Xing, J. Zou, G. Lu and L. A. Wang, *Phys. Chem. Chem. Phys.* 2013, **15**, 12314.
33 A. M. Jubb and H. C. Allen, *ACS Appl. Mater. Interfaces*, 2010, **2**, 2804.
34 L. A. Marusak, R. Messier and W. B. White, *J. Phys. Chem. Solids*, 1980, **41**, 981.
35 V. Cristino, S. Berardi, S. Caramori, R. Argazzi, S. Carli, L. Meda, A. Tacca and C. A. Bignozzi, *Phys. Chem. Chem. Phys.*, 2013, **15**, 13083.
36 B. Klahr, A. B. Martinson and T. W. Hamann, *Langmuir*, 2011, **27**, 461.
37 D. Guyomard, *Journal de Chimie Physique*, 1986, **83**, 355.
38 In eqn (2), J is the photocurrent density, Φ_0 the incident photon flux, α the absorption coefficient, ε_0 and ε the vacuum and semiconductor permittivity, N the donor density, V the applied potential and V_{fb} the flat band potential.
39 L. M. Peter, *J. Solid State Electrochem.*, 2013, **17**, 315.
40 K. G. Upul Wijayantha, S. Saremi-Yarahmadi and L. M. Peter, *Phys. Chem. Chem. Phys.*, 2011, **13**, 5264.
41 B. Klahr, S. Gimenez, F. Fabregat-Santiago, J. Bisquert and T. W. Hamann, *Energy Environ. Sci.,* 2012, **5**, 7626.
42 B. Klahr, S. Gimenez, F. Fabregat-Santiago, J. Bisquert and T. W. Hamann, *J. Am. Chem. Soc.*, 2012, **134**, 16693.
43 L. Badia-Bou, E. Mas-Marza, P. Rodenas, E. M. Barea, F. Fabregat-Santiago, S. Gimenez, E. Peris and J. Bisquert, *J. Phys. Chem. C*, 2013, **117**, 3826.
44 J. A. Glasscock, P. R. F. Barnes, I. Plumb, A. Bendavid and P. J. Martin, *Thin Solid Films*, 2008, **516**, 1716.
45 G. Oskam, D. Vanmaekelbergh and J. J. Kelly, *J. Electroanal. Chem.*, 1991, 315, 65.
46 M. Zhang, W. Luo, N. Zhang, Z. Li T. Yu and Z. Zou, *Electrochem. Comm.*, 2012, **23**, 41.
47 B. S. Zou and V. Volkov, *J. Phys. Chem. Solids*, 2000, **61**, 757.
48 A. Kay, I. Cesar and M. Grätzel, *J. Am. Chem. Soc.*, 2006, **128**, 15714.
49 J. Bandara, J. A. Mielczarski and J. Kiwi, *Langmuir*, 1999, **15**, 7670.